An Efficient Nanophotonic Hot Electron Solar-Blind UV Detector

Zhiyuan Wang, Xiaoxin Wang, Jifeng Liu*

Thayer School of Engineering, Dartmouth College, 14 Engineering Drive, Hanover, New Hampshire, 03755, USA

Supporting Information Placeholder

ABSTRACT: A solar-blind UV photodetector is designed and fabricated based on a nanophotonic metal-oxide-semiconductor (MOS) structure. A large potential barrier of ~3.8 eV at the metal/oxide interface enables solar-blind UV detection by blocking the electrons excited by visible photons while allowing UVexcited hot electrons to pass through. By selecting metal absorbers with high density of states near the Fermi level and employing photon management in self-assembled pseudo-periodic metal nanostructures, we managed to achieve ~74% spectrally averaged UV absorption at λ =200-300 nm. Furthermore, such a high UV absorption is achieved within the hot electron mean free path of ~50 nm from the metal/oxide interface, effectively facilitating the ballistic transport of the UV-excited hot electrons across the interfacial barrier and improving the overall photocurrent. The device has demonstrated a responsivity of 29 mA/W and an internal quantum efficiency of $\sim 18\%$ at $\lambda = 269$ nm, a significant advance compared to ~1% internal quantum efficiency of existing hot electron photodetectors. The photoresponse to visible light is 3-4 orders lower than the UV responsivity, implementing solar-blind UV detection. These results indicate that photon management in metal absorbers with high density of states near the Fermi level can drastically improve the quantum efficiency of hot electron detectors by >10x compared to existing metal/semiconductor Schottky photodetectors. The same device principle can also be extended to cover other spectral regime inaccessible to conventional Si-based photodetectors.

Key Words: hot electron; photodetector; photon management; solar-blind ultraviolet detection; silicon photonics

Solar-blind ultraviolet (UV) detection refers to photon detection specifically in the UV wavelength range of 200 nm to 320 nm¹⁻⁴ without responding to visible light. With minimal background noises from solar radiation, it has broad applications from homeland security to environmental monitoring, 1,2,5-8 including ozonehole monitoring, flame and electrical discharge detection, 4,9,10 furnace and engine control, chemical and biological reagent sensing, 11 as well as UV astronomy. 12 Currently, there are three technical approaches to achieve solar-blind UV detection: photoconductors/photodiodes based on wide band gap (WBG) semiconductors, 7,8,13 solar-blind band-pass UV filters coupled with Si photodetectors. 14-16 and photoemissive detectors based on UV photocathodes. 17,18 However, these detectors face various disadvantages. For example, the WBG semiconductors for solar-blind UV detection need a band gap larger than 3.8 eV. This requirement poses a significant technical challenge to high quality crystal growths (e.g. diamond and Al_xGa_{1-x}N with x>0.3) and dopants activation. 6,7,17,19 Moreover, the high growth temperature (~ 1000 °C) ^{20,21} also makes these WBG materials incompatible with Si microelectronics processing technology. For solar-blind band-pass UV filters, the lack of high quality optical materials at λ =200-300 nm has made the design and fabrication difficult, limiting the optical bandwidth to ~20 nm. ¹⁴ This narrow bandwidth is not enough to cover the entire solar-blind UV regime of λ =200-300 nm. The delicate optical alignment of such filters with Si photodetectors also negatively affects its performance in field work where vibration and percussion are inevitable. Finally, photoemissive detectors are bulky and fragile vacuum electronic devices and require high operation voltages (>>100 V) to achieve a high quantum efficiency. Such drawbacks have greatly limited the application of these traditional solar-blind UV detection methods.

To address the challenges of existing technologies for solar-blind UV detection, here we present a new scheme utilizing UV-excited hot electrons in a nano-photonic metal-oxide-semiconductor (MOS) structure to generate photocurrent via internal photoemission across the metal/oxide interfacial potential barrier of ~3.8 eV. Electrons excited by visible light, on the other hand, are blocked by this high interfacial barrier and generate no photocurrent, thereby achieving solar-blind UV detection. To overcome the relatively low quantum efficiency (~1%) of existing hot electron photodetectors, we adopt 3 major approaches. (1) Enhancing hot electron generation. Tin (Sn) nanostructures are chosen as the metallic UV absorber due to the significantly higher density of states (DOS) near the Fermi level compared to commonly-used plasmonic metals such as Au and Ag. This feature offers more available electronic states for generating hot electrons with energies greater than the metal/oxide interfacial barrier upon UV excitation. (2) Facilitating hot electron transport via photon management. We further explore the design and fabrication technique of self-assembled pseudo-periodic Sn nanodot arrays as a twodimensional (2D) metal grating in the MOS structure in order to maximize the UV absorption within the distance of hot electron mean free path (~50 nm) from the metal/oxide interface. Such photon management facilitates the ballistic transport of hot electrons across the metal/oxide potential barrier upon UV excitation, enhancing the quantum efficiency of the device. (3) Enhancing hot electron collection. The adopted nanophotonic MOS structure provides much better interfacial defect passivation at the SiO₂/Si interface compared to metal/semiconductor interfaces in hotelectron Schottky detectors, thereby increasing the hot electron collection efficiency across the interface. Simulation based on finite-element-method (FEM) is applied to calculate the optical performance of the Sn nanostructures, which is verified by experimental results. Finally, photocurrent measurement of Sn nanodots/SiO₂/n-Si nanophotonic MOS devices under visible and UV excitation demonstrates the solar-blind UV detection capability. with a UV responsivity ~3 orders of magnitude higher than that of the visible light. Thanks to the high DOS near the Fermi level and the photon management that facilitates hot electron transport, a responsivity up to 29.3 mA/W and an internal quantum efficiency (IQE) of 18% has been achieved at λ =269 nm, representing a >10x improvement in the IQE compared to existing metal/semiconductor Schottky photodetectors. The same device principle can be further extended to cover other spectral regimes beyond the capability of conventional Si-based photodetectors.

RESULTS AND DISCUSSIONS

Device Structure and Working Principle. Fig. 1 schematically shows the band diagram and the working principle of the device. It consists of Sn nanostructures as the active UV absorber, thin SiO₂ as the insulating layer (~10 nm thick), and n-type Si as the substrate (Fig. 1a). The potential barrier height at the Sn/SiO₂ interface, given by $\phi_B=W-\chi$, defines the cutoff wavelength of detection (Fig. 1b). Here the work function of Sn is W=4.7 eV (more details in Supporting Information Section 2) while the electron affinity of SiO₂ is χ =0.9 eV.²² Therefore, we have ϕ _B=4.7-0.9=3.8 eV in these devices. Without UV photon excitation at hv>3.8 eV ($\lambda<326$ nm), there is no electrical conduction between the metal and the n-Si region due to a thick enough SiO2 insulation layer (10-15 nm thick) and the high potential barrier at the Sn/SiO₂ interface, which prevent direct tunneling even with the excitation of visible photons. Note that even if visible photons are directly absorbed by Si, the insulating SiO2 will still leave the circuit open. Therefore, truly solar-blind behavior can be achieved. Upon UV excitation with hv>3.8 eV, the excited hot electrons in the Sn nanostructure gain enough energy to overcome the Sn/SiO₂ interfacial barrier and reach the conduction band of n-Si on the other side of the oxide layer. A positive bias is applied on n-Si to facilitate the hot electron transport (Figs. 1a and b). Furthermore, previous study has shown that Sn has a relatively high density of states (DOS) near its Fermi level compared to other metals such as Au²³ (Fig. S1 in the supplemental information), thereby offering more available electrons for the internal photoemission upon UV excitation to enhance the responsivity. This excitation and hot electron transport process leads to a photocurrent between the metal and the n-Si region. Interestingly, when the high energy hot electron relaxes to the conduction band of Si, in principle the excess kinetic energy of >3 eV is large enough to induce impact ionization and generate another free electron in the conduction band (Fig. 1b).²⁴ While the prototype device presented in this paper is too simple to implement and sustain such multiplication gain, this process could be further engineered in future device design to increase the quantum efficiency and detectivity.

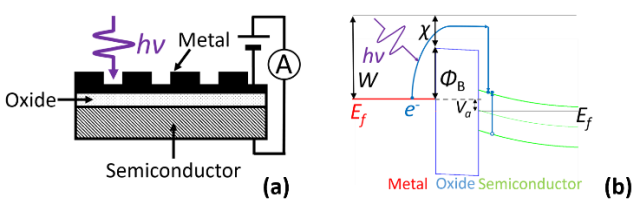


Fig. 1 (a) Schematic cross-sectional profile of the proposed nanophotonic MOS solar-blind UV detector with metallic nanostructures/gratings as the UV absorber. (b) Schematics band diagram of the MOS solar-blind UV detector in (a) under a small positive bias on n-Si. It also shows the process of a hot electron generation upon UV excitation, its transport through the metal/oxide interfacial barrier, and the impact ionization process induced in the semiconductor region due to the excess energy of the hot electron.

Another reason for choosing Sn as the active UV absorber is its high extinction coefficient and plasmonic properties in the UV regime since the efficiency of the proposed nanophotonic MOS photodetector is directly influenced by the UV absorption in the metal region.^{25,26} Note that the metal layer thickness is limited by

the relatively short mean free path of hot electrons with an excess kinetic energy of a few eV.^{27–29} Thus, it is highly desirable to introduce nanophotonic structures in the metal region to enhance UV absorption close to the metal/oxide interface. While nanogratings fabricated by electron beam lithography^{30,31} or nanosphere lithography^{32,33} have been studied, the relatively high cost, slow process and low yield bring challenges into scalable fabrication. In this work, we utilize self-assembled pseudo-periodic Sn nanostructures as a 2D nanophotonic grating, which has high UV absorption in a broad wavelength range and can be produced more conveniently on wafer scale. This fabrication step can be incorporated into the low-temperature back-end-of-line processing during metallization to accommodate the low melting point of Sn.

Self-assembled 2D Nanophotonic Structures. Due to the balance of surface energies, Sn deposited on SiO₂/Si would form nanodots with a thin wetting layer below, following Stranski-Krastanov growth mode. 34,35 The shape and size of as-deposited Sn nanodots are determined by the nominal thickness and the deposition rate. Figs. 2a-c show scanning electron microscope (SEM) images of thermally evaporated Sn with various nominal thickness at the same deposition rate of 0.05 Å/s, as determined in situ with a calibrated quartz crystal monitor. At this relatively low deposition rate (0.05 Å/s). Sn nanodots are formed in all cases. The 2D Fast Fourier Transformation (FFT) spectra, shown in the insets of Figs. 2a-c, reveal the pseudo-periodic character of the Sn nanodots, which becomes more apparent as the nominal thickness increases. The period can be determined by identifying the intensity peak of the first order ring in the FFT spectra, which is similar to the diffraction pattern. Fig. 2d shows that the average period and diameter of the Sn nanodots increase almost linearly with the nominal thickness. With atomic force microscopy (AFM), the profile of the Sn nanodots can be extracted and the average height of Sn nanodots can be estimated. For example, evaporated Sn nanodots with a nominal thickness of 50 nm have an average height of 100 nm. This provides a guideline of fabricating 2D gratings for various working wavelengths.

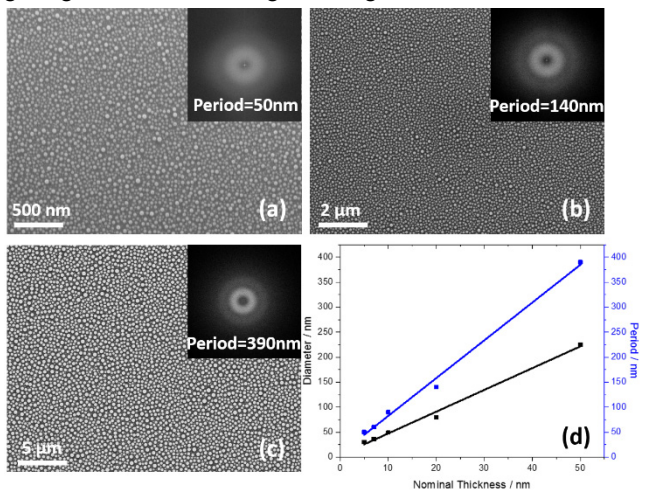


Fig. 2 SEM images of Sn nanostructures with different nominal thicknesses at a deposition rate of 0.05 Å/s: (a) 5 nm, (b) 20 nm and (c) 50 nm. The insets show the FFT spectra of each figure, indicating the average period in each case. (d) Linear fit of Sn dot diameter (the black line) and period (the blue line) versus nominal thickness.

On the other hand, higher deposition rate makes Sn dots larger in size and less circular in shape. For example, for the same 20 nm nominal thickness, Sn deposited at 0.2 Å/s has a period of 180 nm and an average diameter of 150 nm, compared to 140 nm and 80

nm at a deposition rate of 0.05 Å/s (Fig. S3 in supplemental information). This provides another handle to control the period and size of Sn nanodots for desirable optical performance.

Device Modeling

With the geometry and dimensions of Sn nanostructures revealed by microscopy, modeling of Sn nanostructures is performed using finite element method (FEM, COMSOL Wave Optics Module). Hexagonally arranged Sn pellets are used to represent the pseudoperiodic Sn nanodots. As shown in Fig. 3a, the period, radius and height of Sn nanodots are 180 nm, 75 nm and 40 nm, respectively, based on SEM (including FFT analyses) and AFM analyses. Note that similar approximation based on the FFT analysis of pseudoperiodic self-assembled structures has been proved successful in previous literature ^{36,37} because the length scale of the ordering (~µm in this case) is already much larger than the wavelength of interest (~200-300 nm). It is similar to the way that Bloch wave approximation still works well for microcrystalline materials even though the potential is no longer perfectly periodic. Our previous work has also shown clear advantages of using Sn nanostructures vs. continuous thin films in enhancing the UV absorption near the metal/oxide interface to facilitate hot electron transport.³⁸ For the simulation, normal incidence of transverse-magnetic (TM) polarized light is used. However, due to the symmetric geometry for normal incidence, the result is actually independent of polarization. Fig. 3b shows an example of the simulated normalized magnetic field distribution for the Sn nanostructures on SiO₂ (10 nm thick)/Si illuminated at λ =250 nm.

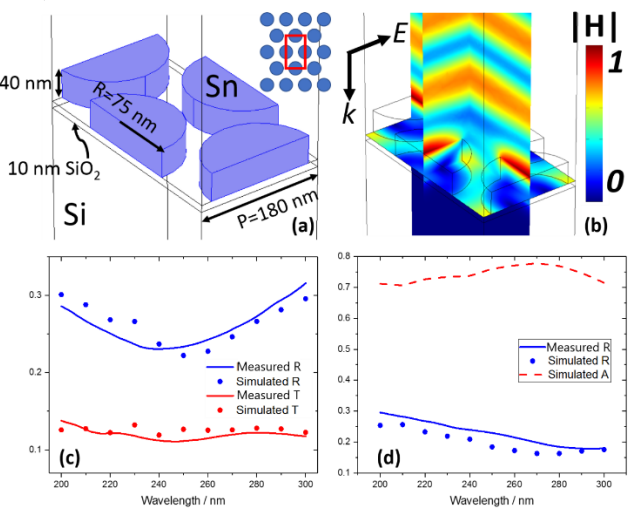


Fig. 3 (a) Schematic figure of the model for Sn nanodots evaporated at $0.2\ \text{Å/s}$ with a nominal thickness of 20 nm. The red rectangle shows the unit cell for modelling. The period of the structure is 180 nm and radius of the Sn nanodots is 75 nm, as revealed by SEM. The height of Sn dots is 40 nm, as revealed by AFM. The substrate is 10 nm thermally grown SiO₂ on Si. The simulation results in (b)-(d) are based on the geometry in (a). (b) Normalized magnetic field distribution around Sn/SiO₂/Si structure with normal incident TM polarized light at a wavelength of 250 nm. (c) Simulated and measured reflectance (in blue) and transmittance (in red) spectra of the Sn nanodots on quartz sample. (d) Simulated and measured reflectance spectra (in blue) of the Sn nanodots on SiO₂/Si. The red dash line shows the simulated absorption of Sn on SiO₂/Si.

The simulated reflectance and transmittance spectra of Sn nandots on quartz agree well with the experimental data (Fig. 3c), so is the reflectance spectrum of Sn nanodots on SiO₂/Si (Fig. 3d). Such a good agreement between modeling and experiment allows us to

evaluate the UV absorption of Sn nanostructures on SiO₂/Si via modeling with reasonable accuracy (see the dashed red line in Fig. 3d), even though it is not possible to tell the absorption of the Sn nanostructures from that of the Si substrate solely from the experimental data. Based on the simulation results, the spectrally averaged UV absorption of the pseudo-periodic Sn nanostructure on SiO_2/Si is 74.1% in the range of λ =200-300 nm, quite remarkable considering that the thickness/height of Sn nanodots is only 40 nm. Note that this thickness is within the mean free path of hot electrons, which greatly facilitates the transport of UV excited hot electrons across the metal/oxide potential barrier, as will be discussed later. To elucidate the mechanism of the high UV absorption, Fig. 3b further shows that the optical field around Sn nanodots is greatly enhanced as a result of the strong localized surface plasmon resonance, thereby contributing to the high UV absorption of the Sn nanostructures. This is further supported by the absorption peak at λ ~250 nm in Fig. S5 of the Supplemental Information.

Photocurrent Measurement and Analysis. Photocurrent measurement is performed by measuring current-voltage (I-V) characteristics with a modulated light source and a lock-in amplifier to minimize the background noise (Fig. 4a). A photo of an exemplary sample with various device sizes is shown in the inset of Fig. 4a. The UV source is provided by a UV light emitting diode (LED) with an emission peak at λ =269 nm and a spectral full width of half maximum of 12 nm. The output power of the LED is 0.71 mW and the light spot area is 0.28 cm². Since the UV LED has a hemispherical collimator lens with a beam divergence of ≤6° and it is kept closed to the sample, the UV light can be considered evenly distributed within the spot. For the visible light source, a fluorescent white light source with a color temperature of 4100 K and a 650 nm wavelength red laser are used. The optical power density of the fluorescent white light source is measured to be 0.98 mW/cm², on the same order as that of the UV LED (2.54 mW/cm²). The spectrum of the fluorescent light is shown in Fig. S6 of the Supporting Information. The output power of the red laser is 3.75 mW and the Gaussian beam spot size is 0.04 cm². The MOS device is placed on a Cu plate with top and bottom probe tips collecting the current. To determine the effective device area, we also measure the capacitance of the device while keeping the same probe position as the I-V measurement. By comparing the experimental and theoretical capacitance values of the Sn nanodot/SiO₂/Si nanophotonic MOS structure, the effective device area used for optical responsivity measurements is determined to be $S=4.2\times10^{-4}$ cm², or $\sim200x200$ um². Then the responsivity of the device under various illumination can be calculated from the photocurrent and the incident optical power on the device area (Fig. 4b).

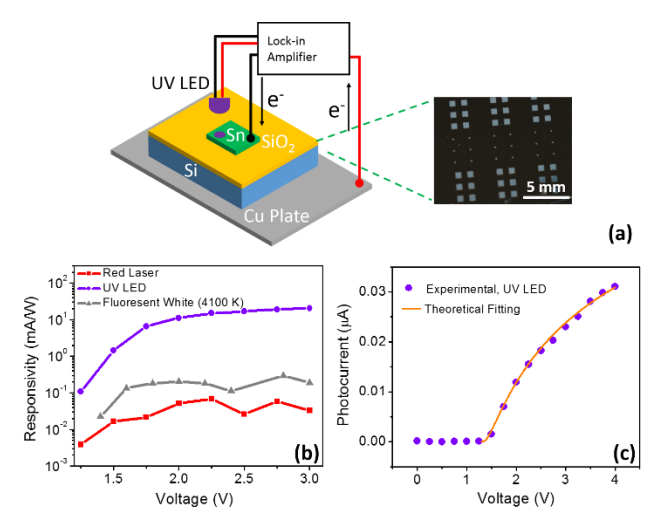


Fig. 4 (a) Schematics of the setup for photocurrent measurement with a lock-in amplifier. The inset of the figure shows the photo of an exemplary sample with different device sizes. (b) Responsivity of the Sn nanodot/SiO₂/Si device under UV LED, red laser, and fluorescent white light excitation (color temperature=4100 K). (c) Comparison of the theoretical and the experimentally measured voltage dependence of the UV photocurrent.

With increasing bias voltage, the responsivity under UV excitation steadily increases as a result of the internal photoemission process of the UV-excited hot electrons, reaching 20.7 mA/W at 3V bias. On the other hand, the responsivity under visible light excitation is 2-3 orders of magnitude lower, i.e. 0.03 mA/W at 3V bias for the red laser and 0.18 mA/W for the fluorescent white light. In fact, the photocurrents measured under the red laser and the fluorescent white light source are both similar to the dark current background, which is on the order of 0.1 nA at 3-4 V bias. Therefore, this visible responsivity is likely limited by the background noise from the electronic equipment. We also find that adding a second layer of Sn nanodots can further improve the UV-to-visible selectivity up to four orders of magnitude, although the absolute UV responsivity is decreased. The details can be found in the Supporting Information, Figs. S8 and S9.

The voltage dependence of the photocurrent agrees with the image force potential well model developed by Berglund and Powell.^{39,40} The theory points out that, for photoinjected electrons with sufficiently large energy (such as the hot electrons excited by UV photons in our case), the voltage dependence of the photoinjected current can be written as:

$$I = A\exp\left[-(V_0/V)^{1/2}\right],\tag{1.1}$$

where

$$V_0 = qd/16\pi\varepsilon_i l^2$$
 and $V = V_a + \phi_1 - \phi_2$

Here A is the scale factor, q is the electron charge, d is the oxide thickness, ε_l is the dielectric constant of the oxide, V_a is the applied voltage, ϕ_1 and ϕ_2 are the barrier energies at the two oxide interfaces (Sn/SiO₂ and SiO₂/Si, respectively), and l is the mean free path for photoinjected electrons in the oxide.

In our case, we modify the applied voltage V_a by an effective voltage offset V_1 . This voltage offset is due to the relatively poor contact between the backside of the device substrate and the current collecting probe. The value of V_1 shall be smaller or near zero as we improve the backside contact in future (such as carefully metallizing the backside of the Si wafer for wire bonding). Now the theoretical photoinjected current is written as:

$$I = A \exp \left\{ -\left[\frac{v_0}{(V_a + \phi_1 - \phi_2 - V_1)} \right]^{\frac{1}{2}} \right\}, \tag{1.2}$$

Fig. 4c shows the experimental and theoretical photocurrent I-V characteristics for our Sn nanodot/SiO₂/Si nanophotonic MOS UV detector, which agrees well with each other. The SiO₂ thickness d is 10 nm and dielectric constant for SiO₂ ε_i is 3.45×10^{-11} F/m. The Sn-Si Schottky barrier height is 0.7 eV according to our measurement in Fig. S2 (see Section 2 of the supporting information), which also equals to $(\phi_2 - \phi_1)/e$. The fitting parameters are A=0.089 μ A, l=0.6 nm and V₁=0.6 V. Previous work shows that for a photoinjected electron with an energy of 5.0 eV, the estimated mean free path in SiO₂ is l=2.6 nm.⁴⁰ Our result indicates a less ideal oxide quality with a smaller mean free path for electrons at similar energy (4.6 eV). Therefore, the hot electron transport and the corresponding UV responsivity could be further improved by optimizing the thin thermal oxide layer.

A UV responsivity of 29.3 mA/W is achieved at 4 V bias. This gives an estimated device external quantum efficiency of EQE=13.5% and an IQE of ~18.0 %, considering the 75.0% UV absorption at λ =269 nm. This performance far exceeds the IQE of typical Schottky interface-based hot electron photodetectors, which is ~1%. ⁴¹⁻⁴⁴ This result proves the effectiveness of the photon management using Sn nanophotonic structures with high DOS near the Fermi level, which greatly improves the UV absorption near the metal/oxide interface to maximize the hot electron excitation and transport process. Compared to metal/semiconductor Schottky detectors, the surface passivation by the 10 nm-thick dry oxide may also play a notable role in reducing interfacial traps and enhancing hot electron transport across the interface.

The noise-equivalent power (NEP) of the device is mainly limited by the dark current due to the less ideal oxide quality, as mentioned earlier in evaluating the mean free path of photo-generated hot electrons in the oxide. It is given by ⁴⁵

$$NEP = \sqrt{2}(h\nu/EQE)(I_D/q)^{1/2},$$
(2.1)

where $h\nu$ is the UV photon energy, EQE is the external quantum efficiency, I_D is the dark current, and q is the electron charge. The corresponding specific detectivity (D*) is given by 45

$$D^* = (S*B)^{1/2}/NEP, (2.2)$$

where S is the device area and B is the bandwidth. Usually NEP and D* are evaluated at B=1 Hz. 45

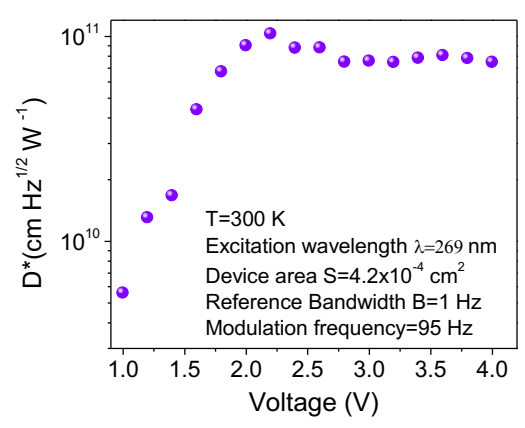


Fig. 5. Specific detectivity vs. applied voltage for the device under an UV excitation wavelength of λ =269 nm.

The specific detectivity vs. applied voltage at a UV excitation wavelength of λ =269 nm is shown in Fig. 5 for a device area of

S=4.2×10⁻⁴ cm². A detectivity on the order of 10¹¹ cm Hz^{1/2} W⁻¹ is achieved at 2-4 V bias. This performance is 1-3 orders better than the metal-semiconductor-metal (Schottky junctions) and metal-insulator-semiconductor solar-blind UV detectors reported earlier, ⁴⁶ demonstrating the effectiveness of our new approach. As mentioned earlier, further improving the oxide quality should reduce traps in the oxide, thereby reducing the dark current and increasing the photocurrent. The absorption enhancement can also be further improved by directly defining gratings on Si substrates and reducing overall metal layer thickness, as suggested by our theoretical modeling. ³⁸ Future design of avalanche gain within this nanophotonic MOS UV detector, or integration with Si quanta image sensor with *room-temperature* photon-counting capability, ⁴⁷ can further improve the sensitivity of these devices.

Conclusions. We demonstrate a nanophotonic solar-blind UV detector that makes use of hot electron excitation and transport in a MOS structure. The potential barrier at the Sn/SiO₂ interface successfully rejects photoresponse from visible photons, enabling a UV responsivity 3-4 orders of magnitude higher than that of the visible light. Self-assembled pseudo-periodic nanostructures of thermally evaporated Sn have been fabricated with desirable periods and sizes to optimize the UV absorption. The high DOS of Sn near the Fermi level and the photon management in the Sn nanostructures greatly improve the efficiency of UV absorption. Strong absorption (~75%) of UV light from 200 nm to 300 nm has been achieved within 40 nm of the Sn/SiO2 interface to facilitate hot electron excitation and transport across the Sn/SiO₂ interfacial barrier. Thanks to the photon management of the Sn nanostructures, the IQE at $\lambda = 260$ nm reaches up to 18%, > 10xhigher than existing metal/semiconductor Schottky photodetectors. This device utilizes simple, Si-process compatible materials and facilities, making it easy to fabricate and integrate with Si read-out integrated circuits (ROICs) compared to existing solarblind UV detection schemes. The same device principle can be further extended to hot electron MOS IR detectors to cover the spectral regimes inaccessible to conventional Si-based photodetectors.

METHODS

Sn Nanodot Deposition. Sn nanodots are thermally evaporated on $\rm SiO_2/Si$ substrates using a Kurt Lesker Lab 18 physical vapor deposition system. The base vacuum of the system is ${\sim}3{\times}10^{-8}$ Torr.

Morphological Characterization. Tescan Vega3 thermionic emitter scanning electron microscope (SEM) is used in the geometry and dimension characterization of Sn dots, i.e. Fig. 2a-c. Statistical data of the diameters of Sn nanodots and the gaps between the Sn nanodots (i.e. Fig. 2d) are obtained by FFT. The results have been furthered confirmed by manually measuring random Sn dots on the SEM images of each sample. Veeco/Digital Instruments Dimension 3100 Atomic Force Microscopy (AFM) is used in the morphological characterizations, i.e. Fig. S4. Tapping mode is used in all cases.

Device Fabrication. We fabricate the devices in the following procedure: first, 10 nm SiO₂ is grown on RCA cleaned n-Si (001) substrates (average resistivity=0.04 ohm cm) by dry oxidation at 1000 °C for 15 minutes, followed by N₂ annealing at 1000 °C for 1 hour to improve the interface quality.⁴⁸ Then Sn nanostructures with a nominal thickness of 20 nm is evaporated at 0.2 Å/s onto the SiO₂ layer. For solar-blind UV detectors, the Sn nanostruc-

tures are deposited through various sizes of mask openings ranging from $50x50~\mu\text{m}^2$ to $2x2~m\text{m}^2$. The deposition rate and nominal thickness have been chosen to achieve the desired nanostructures (i.e. nanodot diameter and period). The same deposition has also been carried out on quartz substrates for optical characterization of the Sn nanodots. From SEM and AFM images, the average period, nanodot diameter, and height of the Sn nanostructures are characterized (see Fig. 2 and Figs. S3 and S4 in the Supporting Information).

Device Optical Characterization. The transmittance and reflectance spectra from λ =200 nm to 300 nm are measured by a Jasco V-570 spectrometer equipped with a Jasco ISN-470 integrating sphere. The absorption is derived as:

Absorption = 1-transmittance-reflectance (1.3)

ACKNOWLEDGMENT

This work has been sponsored by National Science Foundation under the research awards #1700909 and #1231701. We greatly appreciate the help from Dr. Charles Daghlian with the Electron Microscope Facility at Dartmouth College. We thank Dr. Christopher Levey for helping with device fabrication. We thank Dr. Tso-Ping Ma and Dr. Eric Fossum for helping with device capacitance-voltage measurements.

AUTHOR INFORMATION NOTES

Corresponding Author:

*E-mail: <u>Jifeng.Liu@dartmouth.edu</u> ORCID: Jifeng Liu: 0000-0003-4379-2928

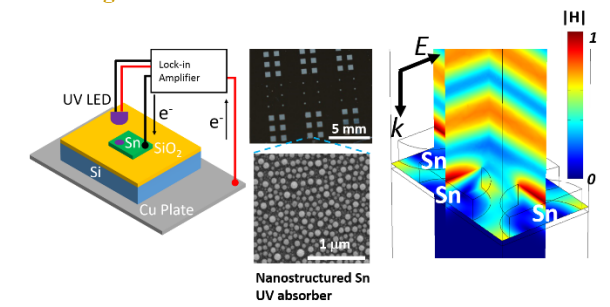
The authors declare no competing financial interest.

ASSOCIATED CONTENT

Supporting Information is provided.

Photoemission spectra from the valence bands of Sn and Au demonstrating the DOS of electrons in these materials, I-V characteristics of Sn/Si Schottky diodes for deriving the Schottky barrier height, SEM images of nominally 20 nm-thick Sn with different deposition rates, AFM analyses on patterned Sn to determine the heights of the Sn nanodots, absorption spectrum of the 20 nm Sn/quartz sample in a broader spectral regime of λ =200-800 nm, emission spectrum of the fluorescent white light source, comparison of the measured C-V curve with the theoretical one for a Sn/SiO₂/Si MOS structure, SEM image and optical spectra of two-step deposited Sn nanodot samples, and the UV and visible responsivity of a typical two-step deposited Sn/SiO₂/Si device are presented in Fig S1-S9, respectively.

ToC Figure



REFERENCES

- Razeghi, M. Short-Wavelength Solar-Blind Detectors -Status, Prospects, and Markets. *Proc. IEEE* 2002, 90 (6), 1006–1014.
- (2) Schreiber, P.; Dang, T.; Pickenpaugh, T.; Smith, G. A.; Gehred, P.; Litton, C. W. Solar-Blind UV Region and UV Detector Development Objectives. In *Japanese Journal of Applied Physics*, 1999, Vol. 42, (Part 2, No. 4B), 230-248.
- (3) Razeghi, M.; Rogalski, A. Semiconductor Ultraviolet Detectors. *J. Appl. Phys.* **1996**, *79* (10), 7433–7473.
- (4) Gorokhov, E. V.; Magunov, A. N.; Feshchenko, V. S.; Altukhov, A. A. Solar-Blind UV Flame Detector Based on Natural Diamond. *Instruments Exp. Tech.* 2008, 51 (2), 280–283.
- (5) Sandvik, P.; Mi, K.; Shahedipour, F.; McClintock, R.; Yasan, A.; Kung, P.; Razeghi, M. AlxGa1-xN for Solar-Blind UV Detectors. In *Journal of Crystal Growth*, 2001, Vol. 231, 366–370.
- (6) Udo Schuhle; Jean-Francois Hochedez. Solar-Blind UV Detectors Based on Wide Band Gap Semiconductors. In Solid-State Electronics; Springer New York: New York, NY, 2007, Vol. 51, 1014–1017.
- (7) Khan, M. A.; Shatalov, M.; Maruska, H. P.; Wang, H. M.; Kuokstis, E. III-Nitride UV Devices. *Japanese J. Appl. Physics*, 2005, 44 (10), 7191–7206.
- (8) Sang, L.; Liao, M.; Sumiya, M. A Comprehensive Review of Semiconductor Ultraviolet Photodetectors: From Thin Film to One-Dimensional Nanostructures; Multidisciplinary Digital Publishing Institute (MDPI), 2013; Vol. 13, 10482–10518.
- (9) Oshima, T.; Okuno, T.; Arai, N.; Suzuki, N.; Hino, H.; Fujita, S. Flame Detection by A-Ga2O3-Based Sensor. *Jpn. J. Appl. Phys.* 2009, 48 (1), 011605.
- (10) Lindner, M. Daylight Corona Discharge Imager. In 11th International Symposium on High-Voltage Engineering (ISH 99); IEEE, 1999, 349
- (11) Hudeish, A. Y.; Tan, C. K.; Abdul Aziz, A.; Hassan, Z. A Chemical Sensor Based on AlGaN. *Mater. Sci. Forum* **2006**, *517*, 33–36.
- (12) Ulmer, M. P.; Razeghi, M.; Bigan, E., Ultraviolet Detectors for Astrophysics: Present and Future, *Proc. SPIE* 2397, (24 April 1995)
- (13) Monroy, E.; Omn s, F.; Calle, F. Wide-Bandgap Semiconductor Ultraviolet Photodetectors. Semicond. Sci. Technol. 2003, 18 (4), R33–R51.
- (14) Li, W.-D.; Chou, S. Y. Solar-Blind Deep-UV Band-Pass Filter (250-350nm) Consisting of a Metal Nano-Grid Fabricated by Nanoimprint Lithography. *Opt. Express* 2010, 18 (2), 931–937.
- (15) Lindner, M.; Elstein, S.; Wallace, J.; Lindner, P. Solar-Blind Bandpass Filters for UV Imaging Devices. *Proc. SPIE* 1998, 3302, 176–183.
- (16) Lim, S. H.; Yu, E. T. Ultraviolet and Solar-Blind Spectral Imaging with Subwavelength Transmission

- Gratings. Appl. Phys. Lett. 2009, 95 (16), 161107.
- (17) BenMoussa, A.; Soltani, A.; Haenen, K.; Kroth, U.; Mortet, V.; Barkad, H. A.; Bolsee, D.; Hermans, C.; Richter, M.; De Jaeger, J. C.; et al. New Developments on Diamond Photodetector for VUV Solar Observations. Semicond. Sci. Technol. 2008, 23 (3), 035026.
- (18) Martin, J.; Hink, P. Characterization of a Microchannel Plate Photomultiplier Tube with High Sensitivity GaAs Photocathode. *Signal* **2002**, *35* (40), 1–6.
- (19) Katsuragawa, M.; Sota, S.; Komori, M.; Anbe, C.; Takeuchi, T.; Sakai, H.; Amano, H.; Akasaki, I. Thermal Ionization Energy of Si and Mg in AlGaN. J. Cryst. Growth 1998, 189190, 528–531.
- (20) Mano, H. a; Kasaki, I. a; Pernot, C.; Hirano, A.; Iwaya, M.; Detchprohm, T.; Amano, H.; Akasaki, I. Solar-Blind UV Photodetectors Based on GaN / AlGaN p-i-n Photodiodes. Appl. Phys. 2000, 39 (5), 387–389.
- (21) Mcclintock, R.; Yasan, A.; Mayes, K.; Shiell, D.; Darvish, S. R.; Kung, P.; Razeghi, M. High Quantum Efficiency AlGaN Solar-Blind p-i-n Photodiodes. *Appl. Phys. Lett.* 2004, 84 (10), 1248–2277.
- (22) Robertson, J. Band Offsets of Wide-Band-Gap Oxides and Implications for Future Electronic Devices. *J. Vac. Sci. Technol. B Microelectron. Nanom. Struct.* **2000**, *18* (3), 1785.
- (23) Attekum, P. M. T. M. Van; Trooster, J. M. An X-Ray Photoelectron Spectroscopy of PdSb, PtBi and AuSn. *J. Phys. F Met. Phys.* **1979**, *9* (11), 2287–2300.
- (24) Chang, C.; Hu, C.; Brodersen, R. W. Quantum Yield of Electron Impact Ionization in Silicon. *J. Appl. Phys.* **1985**, *57* (2), 302–309.
- (25) McMahon, J. M.; Schatz, G. C.; Gray, S. K. Plasmonics in the Ultraviolet with the Poor Metals Al, Ga, In, Sn, Tl, Pb, and Bi. *Phys. Chem. Chem. Phys.* **2013**, *15* (15), 5415–5423.
- (26) Takeuchi, K.; Adachi, S. Optical Properties of β-Sn Films. J. Appl. Phys. 2009, 105 (7), 073520.
- (27) Crowell, C. R.; Spitzer, W. G.; Howarth, L. E.; Labate, E. E. Attenuation Length Measurements of Hot Electrons in Metal Films. *Phys. Rev.* **1962**, *127* (6), 2006–2015.
- (28) Sze, S. M.; Moll, J. L.; Sugano, T. Range-Energy Relation of Hot Electrons in Au. *IEEE Trans. Electron Devices* **1963**, *10* (5), 336.
- (29) Stuart, R. N.; Wooten, F.; Spicer, W. E. Mean Free Path of Hot Electrons and Holes in Metals. *Phys. Rev. Lett.* **1963**, *10* (1), 7–9.
- (30) Chalabi, H.; Schoen, D.; Brongersma, M. L. Hot-Electron Photodetection with a Plasmonic Nanostripe Antenna. *Nano Lett.* **2014**, *14* (3), 1374–1380.
- (31) Li, W.; Valentine, J. Metamaterial Perfect Absorber Based Hot Electron Photodetection. *Nano Lett.* **2014**, *14* (6), 3510–3514.
- (32) Zhang, W.; Xu, J.; Ye, W.; Li, Y.; Qi, Z.; Dai, J.; Wu, Z.; Chen, C.; Yin, J.; Li, J.; et al. High-Performance AlGaN Metal-Semiconductor-Metal Solar-Blind Ultraviolet Photodetectors by Localized Surface Plasmon Enhancement. Appl. Phys. Lett. 2015, 106 (2).
- (33) Chan, G. H.; Zhao, J.; Hicks, E. M.; Schatz, G. C.; Van Duyne, R. P. Plasmonic Properties of Copper

- Nanoparticles Fabricated by Nanosphere Lithography. *Nano Lett.* **2007**, *7* (7), 1947–1952.
- (34) Zhao, X.; Wang, K.-F.; Zhang, W.; Huang, M.; Mao, Y. Growth Research of Sn Nanoparticles Deposited on Si(001) Substrate by Solid Phase Epitaxy. *Appl. Surf. Sci.* 2010, 256 (21), 6427–6432.
- (35) Eisenmenger-Sittner, C.; Bangert, H.; Störi, H.; Brenner, J.; Barna, P. B. Stranski-Krastanov Growth of Sn on a Polycrystalline Al Film Surface Initiated by the Wetting of Al by Sn. *Surf. Sci.* **2001**, *489* (1–3), 161–168.
- (36) Sheng, X.; Liu, J; Coronel, N.; Agarwal, A. M.; Michel, J.; Kimerling, L. C. Integration of self-assembled porous alumina and distributed bragg reflector for light trapping in Si photovoltaic devices. *IEEE. J. Photon. Technol. Lett.* **2010**, *22* (18), 1394–1396.
- (37) Sheng, X; Liu, J; Kozinsky, I.; Agarwal, A.M.; Michel, J.; Kimerling, L. C. Design and non-lithographic fabrication of light trapping structures for thin film silicon solar cells. *Adv. Mater.*, **2011**, 23(7), 843–847,.
- (38) Wang, Z.; Wang, X.; Liu, J. Design of Nanophotonic, Hot-Electron Solar-Blind Ultraviolet Detectors with a Metal-Oxide-Semiconductor Structure. J. Opt. 2014, 16 (12), 125010.
- (39) Berglund, C. N.; Powell, R. J. Photoinjection into SiO2: Electron Scattering in the Image Force Potential Well. *J. Appl. Phys.* **1971**, *42* (2), 573–579.
- (40) Powell, R. J. Interface Barrier Energy Determination from Voltage Dependence of Photoinjected Currents. *J. Appl. Phys.* **1970**, *41* (6), 2424–81301.
- (41) Fukuda, M.; Aihara, T.; Yamaguchi, K.; Ling, Y. Y.; Miyaji, K.; Tohyama, M. Light Detection Enhanced by Surface Plasmon Resonance in Metal Film. Appl. Phys. Lett. 2010, 96 (15), 153107.
- (42) Knight, M. W.; Sobhani, H.; Nordlander, P.; Halas, N. J. Photodetection with Active Optical Antennas. *Science*. 2011, 332 (6030), 702–704.
- (43) Akbari, A.; Berini, P. Schottky Contact Surface-Plasmon Detector Integrated with an Asymmetric Metal Stripe Waveguide. Appl. Phys. Lett. 2009, 95 (2), 021104.
- (44) Goykhman, I.; Desiatov, B.; Khurgin, J.; Shappir, J.; Levy, U. Waveguide Based Compact Silicon Schottky Photodetector with Enhanced Responsivity in the Telecom Spectral Band. Opt. Express 2012, 20 (27), 28594–28602.
- (45) Sze, S. M. Physics of Semiconductor Devices, 1981, 2nd edition, Chapter 13, Wiley-Interscience.
- (46) Lin, C.-H.; Liu, C.-W.; Metal-Insulator-Semiconductor Photodetectors. Sensors. **2010**, *10*, 8797-8826.
- (47) Ma, J.; Fossum, E. R. Quanta Image Sensor Jot With Sub 0.3e- r.m.s. Read Noise and Photon Counting Capability. *IEEE Electron Device Lett.* 2015, 36 (9), 926–928.
- (48) Arienzo, M.; Dori, L.; Szabo, T. N. Effect of Post-oxidation Anneal on Ultrathin SiO₂ Gate Oxides. Appl. Phys. Lett. 1986, 49 (16), 1040–1042.

Supporting Information for

An Efficient Nanophotonic Hot Electron Solar-Blind UV Detector

Zhiyuan Wang, Xiaoxin Wang, Jifeng Liu*

Thayer School of Engineering, Dartmouth College, 14 Engineering Drive, Hanover, New Hampshire, 03755, USA

1. The Density of States (DOS) of Sn near the Fermi level

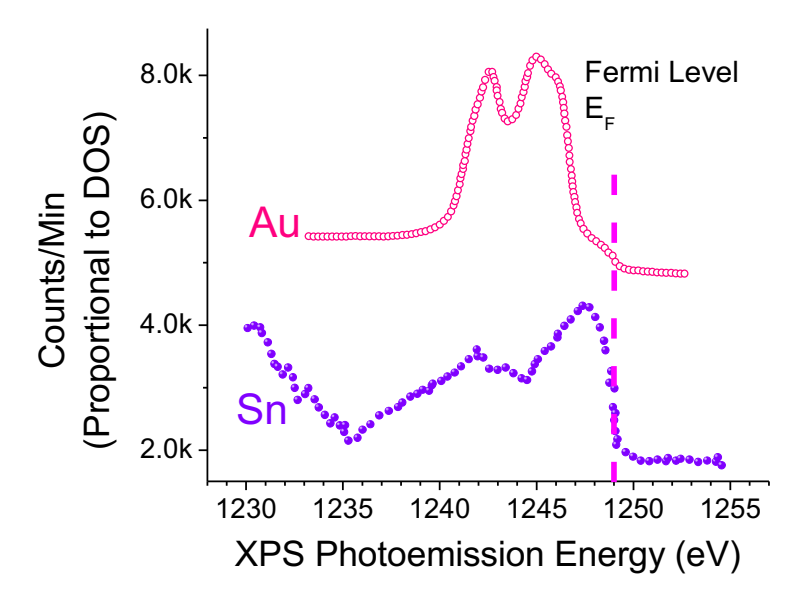


Fig. S1. Photoemission spectra from the valence band of Sn compared to that of Au. The intensity of the photoemission (in counts/min) is proportional to the density of states (DOS). The data are collected from Fig. 3 in Ref. 23 and replotted here. This figure shows that Sn has a relatively high density of states near the Fermi level compared to Au, meaning that that there are a large number of electrons available for the UV excitation and injection across the Sn/SiO_2 interface, as schematically shown in Fig. 1b of the main text. Therefore, the high DOS near the Fermi level in Sn enhances the absorption of UV photons with energies close to the metal/oxide barrier height (Φ_B) .

2. Measuring the Work Function of Thermally Evaporated Sn

Although one study gives the work function of Sn as W_{Sn} =4.42 eV, ^{S1} the actual result is dependent on several factors, including sample surface morphology, crystallinity, facet of the contact plane, and method of measurement. In Ref. S1, Sn is a polycrystalline thin film with unknown thickness and the method is to measure contact potential difference with Al. Another study performs scanning Kelvin probe measurement and ultraviolet photoelectron spectroscopy on bulk polycrystalline Sn, obtaining a work function of 4.47±0.008 eV and 4.14±0.19 eV, respectively. ^{S2} With different preparation methods, surface morphology of the sample and measurement methods, the actual value of Sn work function could be different. ^{S2-S6} So it is necessary to measure the work function of the Sn nanostructures fabricated and tested in this work.

To determine the work function of Sn, Sn on Si Schottky junction samples are prepared. The substrate is phosphorus-doped N-type <100> Si with an average resistivity of 0.04 ohm cm. This gives an n-type doping concentration of 3.4×10^{17} cm⁻³. The electron affinity of Si is χ_{Si} =4.03 eV. Based on the Schottky barrier height of Sn/Si junction, given by Φ_{Sn-Si} =W_{Sn- χ_{Si}}, the work function of Sn can be calculated.

The fitting is based on the conventional Schottky barrier thermionic emission theory model: S7

$$I = I_0 \left[\exp\left(\frac{q(V - IRS)}{nkT}\right) - 1 \right], \tag{S1.1}$$

where I_0 is the saturation current, n is the ideality factor and R_s is the series resistance. The saturation current I_0 is given by

$$I_0 = AA^*T^2 exp\left(-\frac{q\phi_B}{kT}\right), \tag{S1.2}$$

where A is the contact area, A^* is the Richardson constant and ϕ_B is the Schottky barrier height.

For nominally 50 nm and 100 nm-thick Sn deposited on Si, the Schottky barrier heights obtained by fitting the I-V data in Fig. S2 are 0.73 eV and 0.71 eV respectively. This means the work function of Sn should be around 4.74~4.76 eV. The higher work function compared to the bulk Sn material is likely due to the formation of Sn nanodots in our case.

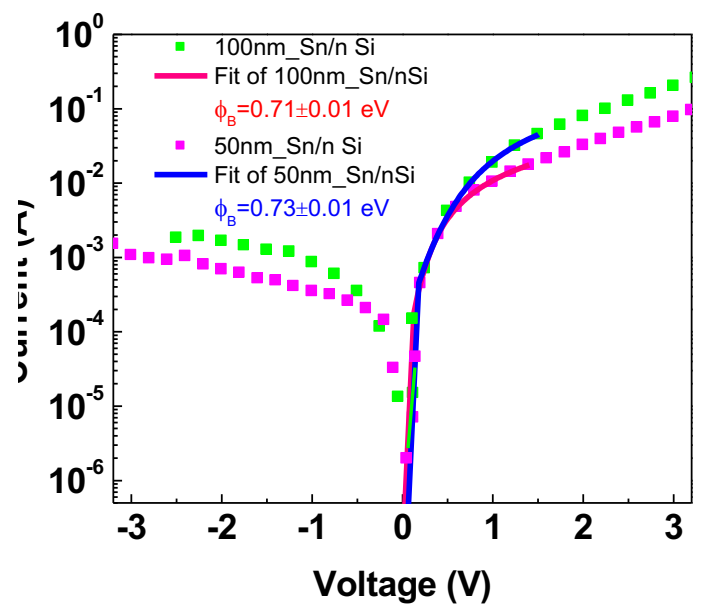


Fig. S2. I-V characteristics of two Schottky junctions: 50 nm Sn and 100 nm on Si. The curve fitting using Eq. S1 yields Schottky barrier heights of ~0.7 eV in both cases.

3. Morphology of Sn nanodots deposited at various rates.

Fig. S3 shows SEM images of Sn deposited at different rates for the same nominal thickness of 20 nm. The deposition rates are 0.05 Å/s, 0.1 Å/s, 0.2 Å/s and 0.4 Å/s, respectively, for Fig S3a-c. For Sn deposited at relatively low rates $(0.05 \sim 0.1 \text{ Å/s})$, the average diameter is 80 nm and period is around 140 nm. With increasing deposition rate, the average diameter increases to $140 \sim 150 \text{ nm}$ and the period also increases to $180 \sim 200 \text{ nm}$.

We believe this is result of the annealing affect during evaporation. Previous research has shown that surface temperate will affect Sn morphology during deposition, ^{S8} as well as post-deposition annealing of deposited Sn. ^{S9} In this work, faster deposition rate means less surface diffusion of Sn atoms, thus less annealing effect. Therefore, Sn deposited at higher rate (0.2~0.4 Å/s) appears less circular and more flattened.

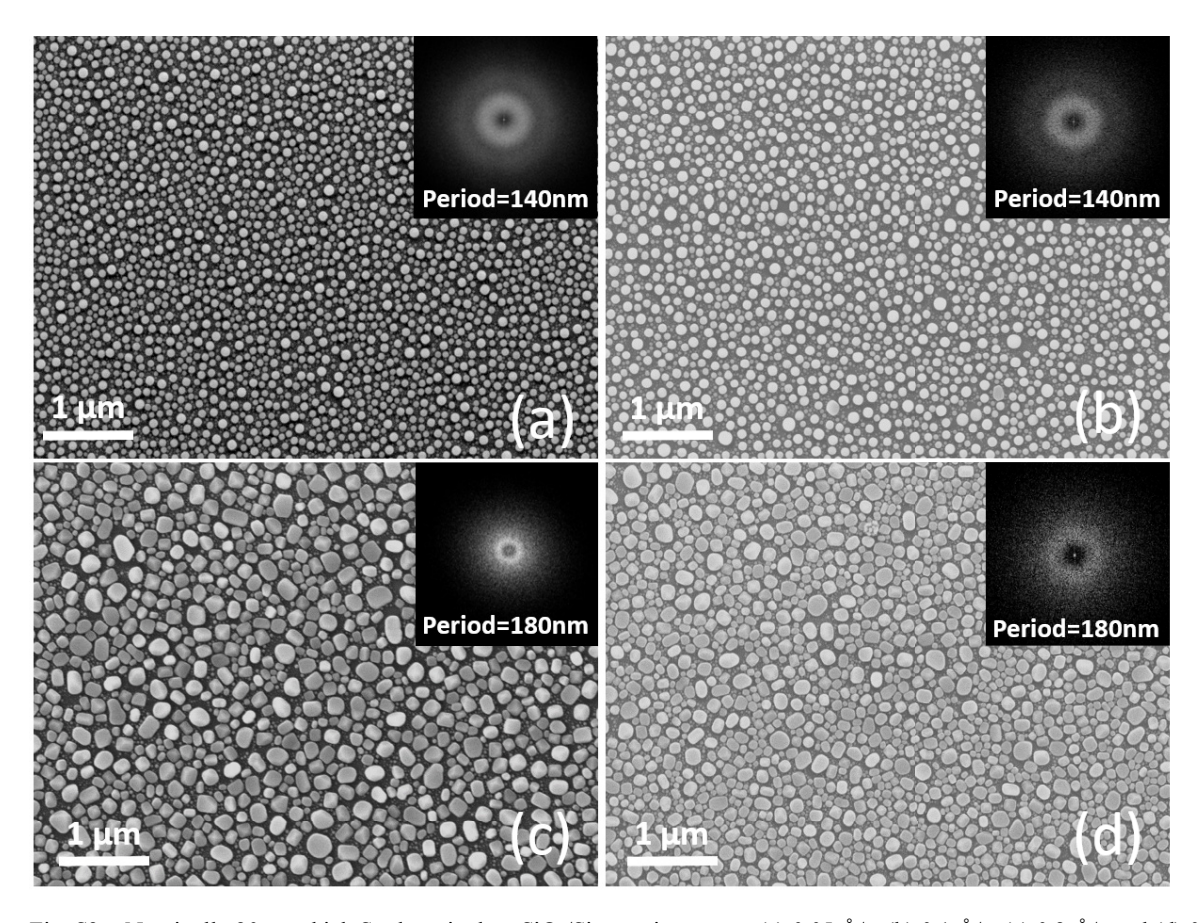


Fig. S3. Nominally 20 nm-thick Sn deposited on SiO_2/Si at various rates: (a) 0.05 Å/s, (b) 0.1 Å/s, (c) 0.2 Å/s and (d) 0.4 Å/s. The insets of the figures show the Fast Fourier Transform (FFT) images of the SEM images, indicating the pseudo periodicity of the self-assembled Sn nanodots.

4. AFM measurement of Sn nanostructures.

AFM measurement provides information about the surface morphology of the deposited Sn nanostructures and the height of the Sn nanodots. The sample is patterned by photolithography and lift-off process. This leaves trenches where no Sn is deposited so that the height of the Sn dots can be precisely measured by investigating the surface profile across the boundary between the regions with and without Sn nanodots (see lines 1-3 in Fig. S4). This profile extraction shows that the average height of Sn nanodots is ~40 nm.

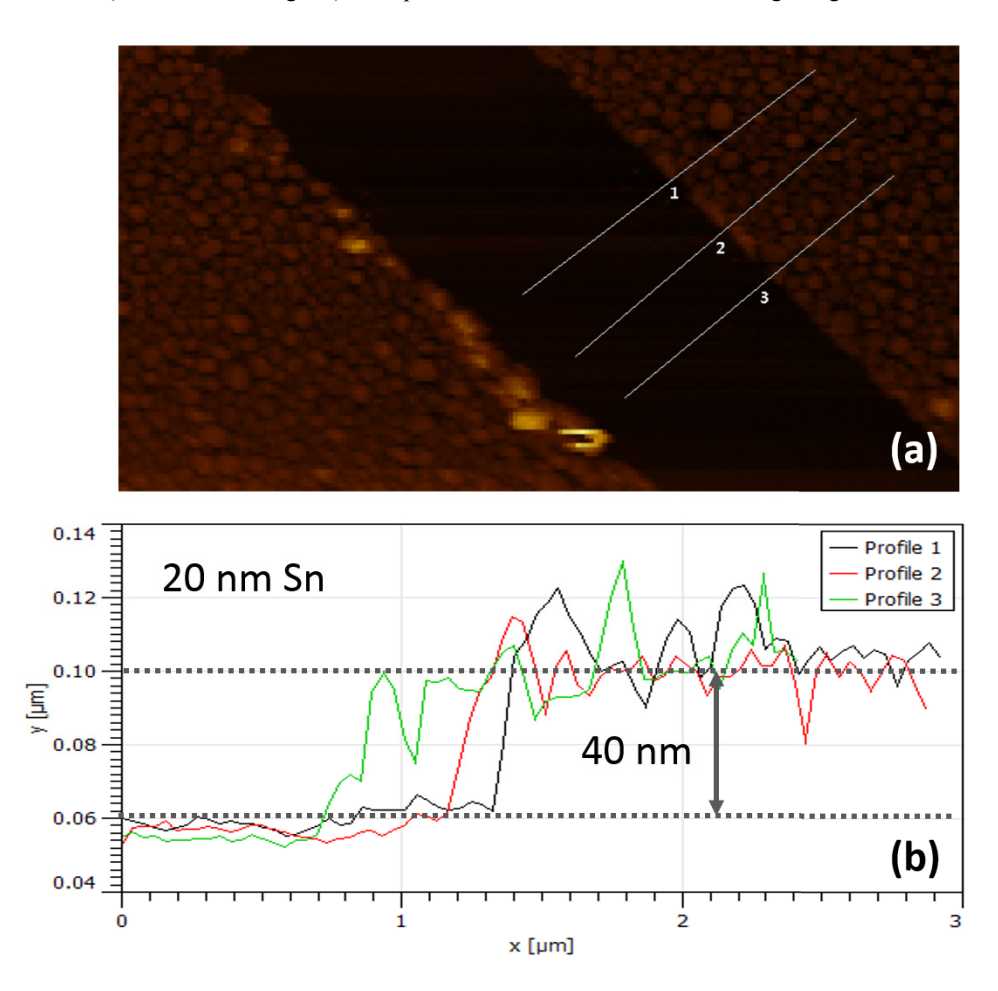


Fig. S4. (a) AFM measurement on patterned Sn nanodots. Lines 1-3 indicate the locations of three measurements across the boundary between the regions with and without Sn nanodots. (b) Surface profile extraction across the boundary between the regions with and without Sn nanodots at lines 1-3 in (a).

5. Absorption spectrum of the 20 nm Sn/quartz sample in a broader spectral regime

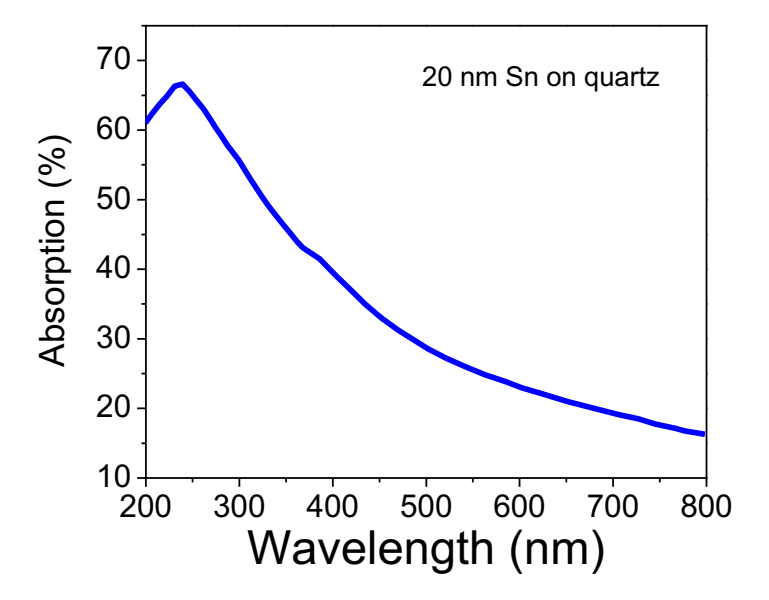


Fig. S5. Absorption spectrum of the 20 nm Sn/quartz sample at λ =200-800 nm. An absorption peak is clearly observed at λ ~250 nm.

6. Optical Emission Spectrum of the Fluorescent White Light Source

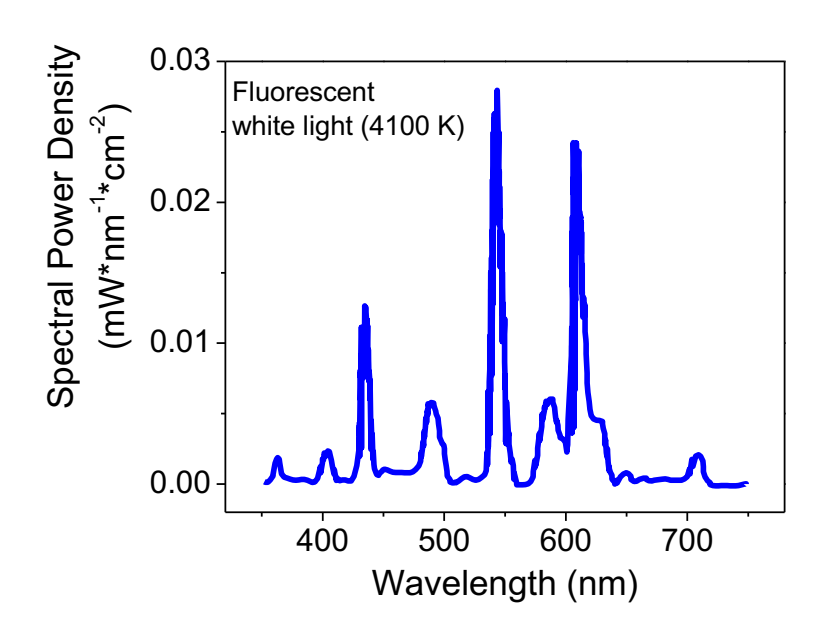


Fig. S6. Optical emission spectrum of the fluorescent white light source with a color temperature of 4100 K.

7. Capacitance-Voltage Measurement

Capacitance-voltage (C-V) characteristics of the Sn nanodots/SiO₂/Si MOS device is measured and compared with the theoretical value to determine the effective contact area of the device. Theoretical C-V is calculated using MOSCap, a simulation tool for MOS capacitor modelling. The dielectric constant of the gate oxide is set to 3.9 while the work function of Sn is set to 4.7 eV (according to the results in Fig. S2). The doping level for N-type Si substrate is set to 3.4×10¹⁷ cm⁻³ based on the resistivity of the Si substrate (0.04 ohm cm on average).

To maintain the same condition of electrical contacts as the photocurrent I-V measurements, we perform C-V measurement right after each photocurrent measurement, keeping the probe tip at exactly at the same position. In this way, the effective device area can be derived from the C-V data for each photocurrent measurement, which is then used to calculate the responsivity and quantum efficiency.

Fig. S5 shows an example of the measured vs. the simulated C-V curves. The metal contact is consisted of two-step deposited Sn (20+20 nm). The metal contact size is 4 mm \times 5 mm. The C-V measurement is carried out with a LCR meter (HP 4284A). The frequency is set to 1000 Hz. The general trend of C-V agrees well with theoretical result, indicating that the oxide of the device has reasonably good electrical quality.

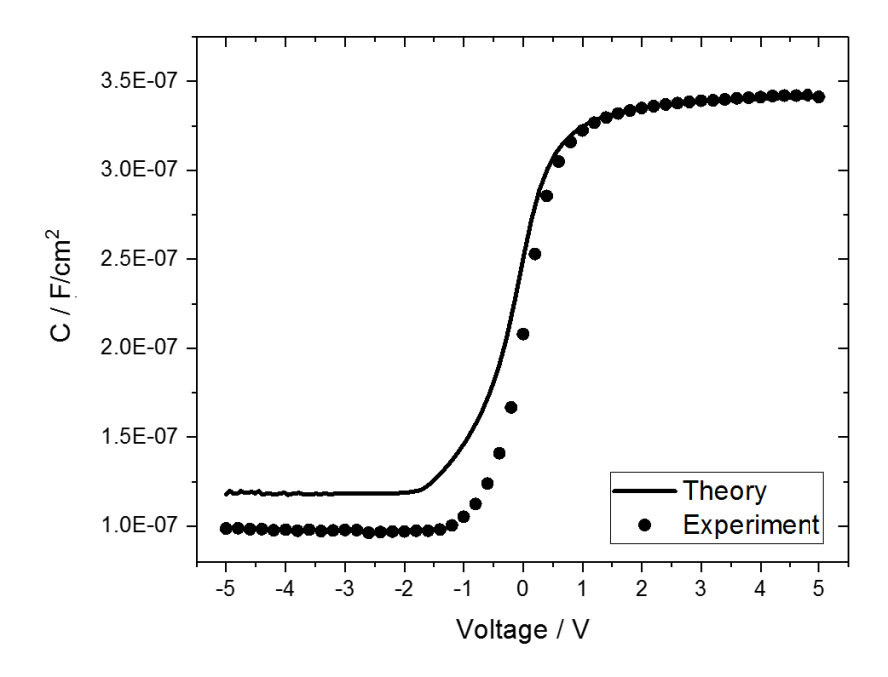


Fig. S7. Comparison of measured C-V curve with theoretical C-V curve of a Sn/SiO₂/Si MOS structure

8. Two-step Sn deposition and Optoelectronic Characterization.

We attempted a two-step deposition method to further engineer the UV selectivity. After the sample is deposited with Sn and cools down to room temperature, the same deposition process is repeated as a second-step deposition. Compared to continuous deposition which forms larger nanodots, this method produces two groups of Sn nanodots with similar pseudo-periodic characteristics (Fig. S6a). FFT result shows that the two-step deposition has a period of 160 nm, slightly larger than that of the single-deposition case in Fig. 2b (140 nm). With Sn dots in the second step of deposition filling the gaps of first step, the coverage of Sn dots is improved to reduce the direct exposure of Si to visible photon excitation, which could generate a small amount of tunneling current assisted by visible photons. On the other hand, we did observe some stacked Sn dots which could unwantedly increase the transport path length of UV-excited hot electrons. Overall, we would expect a higher UV-to-visible spectral selectivity at the cost of lower absolute responsivity. This expectation has been confirmed by experimental results, as will be discussed shortly.

Similar modelling and optical characterization have also been carried out on the two-step deposited Sn samples (Figs S6 b-d). The result shows that it has a spectrally averaged absorption of 75.6% from 200 nm to 300 nm.

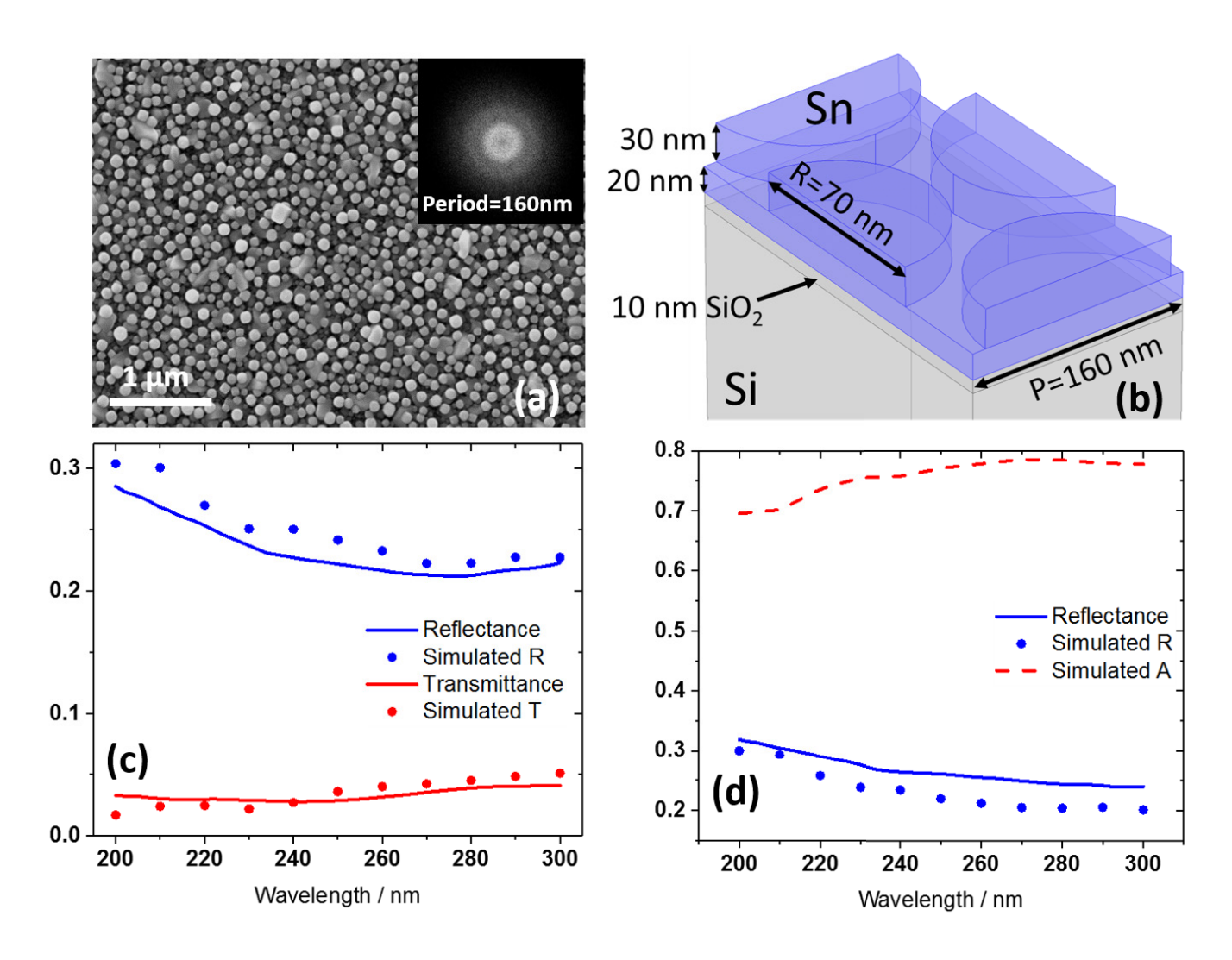


Fig. S8. (a) SEM image of two-step deposited Sn sample. The FFT analysis in the inset shows a pseudo period of 160 nm. (b) Model for two-step deposited Sn with parameters from SEM and AFM measurements. (c) Simulated and measured reflectance and transmittance of Sn on quartz sample. (d) Simulated and measured reflectance of Sn on SiO_2/Si sample. The red dash line is the simulated absorption of Sn on SiO_2/Si .

As expected, photocurrent measurement in Fig. S7 on two-step deposited Sn samples indeed shows higher UV-to-visible spectral selectivity at the cost of smaller responsivity compared to the samples with single-step deposited Sn nanodots. The responsivities for UV and visi-

ble light are 1.33 mA/W at λ =260 nm and 0.25 μ A/W at λ =650 nm, respectively. On the other hand, the selectivity between UV and visible is improved, up to 4 orders of magnitude versus 3 orders in single-step deposited Sn samples. The trade-off between UV responsivity and spectral selectivity can be further optimized by tuning the height of the Sn nanodots via the nominal Sn layer thickness.

The voltage dependence of photocurrent is similar to one-layer Sn, too (Fig. S7b). The fitting parameters are l=1.24 nm, A=0.0055 μA and $V_1=0.97$ V. The different estimated mean free path of hot electrons in SiO₂ in two-step vs. single-step deposited Sn nanodot samples also indicates that there is variation of SiO₂ quality from different devices, which can be further improved and optimized.

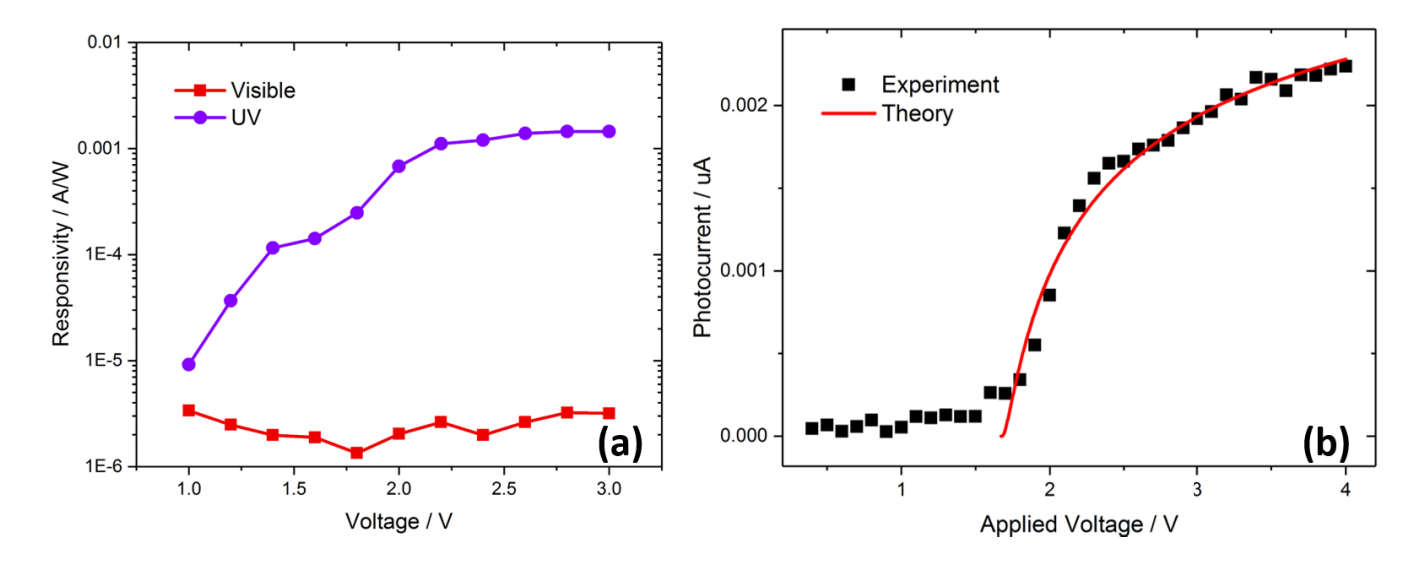


Fig. S9. (a) UV and visible responsivity of a typical two-step deposited $Sn/SiO_2/Si$ device. (b) Comparison of theoretical and measured voltage dependence of UV photocurrent.

References of the Supplementary Information

- (S1) Skriver, H. L.; Rosengaard, N. M. Surface Energy and Work Function of Elemental Metals. *Phys. Rev. B* **1992**, *46* (11), 7157–7168
- (S2) Orf, N. D.; Baikie, I. D.; Shapira, O.; Fink, Y. Work Function Engineering in Low-Temperature Metals. *Appl. Phys. Lett.* **2009**, 94 (11), 113504.
- (S3) Michaelson, H. B. The Work Function of the Elements and Its Periodicity. J. Appl. Phys. 1977, 48 (11), 4729–4733.
- (S4) Baikie, I. D.; Van Der Werf, K. O.; Oerbekke, H.; Broeze, J.; Van Silfhout, A. Automatic Kelvin Probe Compatible with Ultrahigh Vacuum. *Rev. Sci. Instrum.* **1989**, *60* (5), 930–934.
- (S5) Kim, J. S.; Lägel, B.; Moons, E.; Johansson, N.; Baikie, I. D.; Salaneck, W. R.; Friend, R. H.; Cacialli, F. Kelvin Probe and Ultraviolet Photoemission Measurements of Indium Tin Oxide Work Function: A Comparison. *Synth. Met.* **2000**, *111*, 311–314.
- (S6) M. Cardona; Ley, L. Fermi Surface Excitations in X-Ray Photoemission Line Shapes from Metals, *Photoemission in Solids I*, 1978, Vol. 26, 197.
- (S7) Crowell, C. R. The Richardson Constant for Thermionic Emission in Schottky Barrier Diodes. *Solid. State. Electron.* **1965**, *8* (4), 395–399.
- (S8) Chen, P. J.; Colaianni, M. L.; Yates, J. T.; Arbab, M. Thermal Properties of the Sn/SiO2 Interface as Studied by Surface Spectroscopies. *J. Non. Cryst. Solids.* **1993**, *155* (2), 131–140.
- (S9) Kim, J.; Battaglia, C.; Charrière, M.; Hong, A.; Jung, W.; Park, H.; Ballif, C.; Sadana, D. 9.4% Efficient Amorphous Silicon Solar Cell on High Aspect-Ratio Glass Microcones. *Adv. Mater.* **2014**, *26* (24), 4082–4086.
- (S10) Akira Matsudaira, Saumitra Raj Mehrotra, Shaikh S. Ahmed, Gerhard Klimeck, D. V. MOSCap.